PNAS RESEARCH ARTICLE | EARTH, ATMOSPHERIC, AND PLANETARY SCIENCES

High abundance of solar wind-derived water in lunar soils from the middle latitude

Yuchen Xu[a,1], Heng-Ci Tian[b,1], Chi Zhang[b], Marc Chaussidon[c], Yangting Lin[b,2], Jialong Hao[b], Ruiying Li[b], Lixin Gu[b], Wei Yang[b], Liying Huang[a], Jun Du[a], Yazhou Yang[a], Yang Liu[a], Huaiyu He[d], Yongliao Zou[a], Xianhua Li[d], and Fuyuan Wu[d]

Edited by Mark Thiemens, University of California, San Diego, La Jolla, CA; received August 22, 2022; accepted November 8, 2022

Remote sensing data revealed that the presence of water (OH/H_2O) on the Moon is latitude-dependent and probably time-of-day variation, suggesting a solar wind (SW)-originated water with a high degassing loss rate on the lunar surface. However, it is unknown whether or not the SW-derived water in lunar soil grains can be preserved beneath the surface. We report ion microprobe analyses of hydrogen abundances, and deuterium/hydrogen ratios of the lunar soil grains returned by the Chang'e-5 mission from a higher latitude than previous missions. Most of the grain rims (topmost ~100 nm) show high abundances of hydrogen (1,116 to 2,516 ppm) with extremely low δD values (−908 to −992‰), implying nearly exclusively a SW origin. The hydrogen-content depth distribution in the grain rims is phase-dependent, either bell-shaped for glass or monotonic decrease for mineral grains. This reveals the dynamic equilibrium between implantation and outgassing of SW-hydrogen in soil grains on the lunar surface. Heating experiments on a subset of the grains further demonstrate that the SW-implanted hydrogen could be preserved after burial. By comparing with the Apollo data, both observations and simulations provide constraints on the governing role of temperature (latitude) on hydrogen implantation/migration in lunar soils. We predict an even higher abundance of hydrogen in the grain rims in the lunar polar regions (average ~9,500 ppm), which corresponds to an estimation of the bulk water content of ~560 ppm in the polar soils assuming the same grain size distribution as Apollo soils, consistent with the orbit remote sensing result.

solar wind | lunar soil | Chang'e-5 mission | ion microprobe | water

Significance

The latitude-dependent and probably time-of-day variations of water (OH/H_2O) on the Moon surface have previously been explored by reflectance spectroscopy. The lunar soils returned by the Chang'e-5 mission from a middle latitude, significantly higher than Apollo missions, provide a unique opportunity for studying the latitude-dependent implantation and retention of solar wind (SW)-derived water in lunar soils. We have conducted a combined NanoSIMS–FIB–TEM analysis of the CE-5 soil grains, complemented by the heating experiments. The high abundance of SW-derived hydrogen in the rims of the grains provides a significant constraint on the preservation of SW-derived water in lunar soils. The predicted water contents of bulk soils in the lunar polar regions are consistent with the remote sensing data.

The global Moon is covered by a layer of soil-like fine-grained materials, up to ~12 to 15 m in thickness (1–3), called the lunar regolith and produced mainly by asteroid/comet impacts (4). During their formation, lunar soils accumulated hydrogen (in the form of H, H_2, OH, and H_2O) mainly via asteroid/comet impacts (5, 6), volcanic outgassing (7–9), and solar wind (SW) implantation (6, 10–13). The exploration of the lunar surface by orbital near-infrared spectroscopy led to the discovery of water (OH/H_2O) absorption features, which exhibit latitude-dependent (14, 15) and time-of-day variations (15, 16). However, due to the limited optical sensitivity of this technique, these signals cannot be extended to depths below ~1 mm. In fact, observations of diurnal water-abundance changes of up to 200 ppm (15) suggest a very fast desorption rate from the lunar surface. In this case, SW-derived water could be largely lost from the surface soils via temperature-dependent diffusion and outgassing when SW implantation is stopped by shielding with only a single micron-sized grain layer or turn-over caused by impacts. In addition, hydrogen migration on the surface of the Moon was indicated by neutron spectrometry, which can probe hydrogen up to ~0.5 m in depth and found high hydrogen concentrations at lunar poles, suggestive of the presence of water frost/ice in the permanently shadowed craters (17). There was no correlation between the hydration feature in the reflectance spectra and the hydrogen abundance determined by neutron spectrometry, demonstrating that the formation and temporary retention of OH/H_2O are most likely ongoing surficial processes (14). These processes may also lead to migration of water toward the poles and then accumulation in the permanently shadowed regions of the Moon (14, 18, 19). However, the hydration and dehydration processes of SW-implanted OH/H_2O taking place on the topmost surface of individual lunar soil grains, and the possible changes when buried at depth, remain largely unknown.

The studies of Apollo samples revealed that SW-H was a major contributor to the surficial water of the Moon (6, 10–13). The main occurrences of lunar surficial water include adsorbed and/or vapor-deposited OH/H_2O on grain surfaces, SW-produced OH/H_2O in the grain rims, and OH/H_2O in shock-induced melts. While water is stable in the shock-induced melts, the directly implanted SW-H, when not chemically bonded to

Author contributions: Y. Lin designed research; Y.X., H.-C.T., and C.Z. performed research; Y.X., H.-C.T., M.C., Y. Lin, J.H., R.L., L.G., W.Y., L.H., J.D., and Y.Y. analyzed data; and Y.X., H.-C.T., C.Z., M.C., Y. Lin, Y. Liu, H.H., Y.Z., X.L., and F.W. wrote the paper.

The authors declare no competing interest.

This article is a PNAS Direct Submission.

[1]Y.X. and H.-C.T. contributed equally to this work.

[2]To whom correspondence may be addressed. Email: LinYT@mail.iggcas.ac.cn.

This article contains supporting information online at https://www.pnas.org/lookup/suppl/doi:10.1073/pnas.2214395119/-/DCSupplemental.

Published December 12, 2022.

oxygen to form OH/H_2O, could be largely lost from lunar soil grains by diffusion and outgassing (20–22). The outgassing could be more significant for the Apollo lunar soils due to high surface temperatures at low latitudes on the Moon. Different from all six Apollo and three Luna missions, which landed at low latitudes (8.97°S to 26.13°N), the Chang'e-5 (hereafter CE-5) mission returned soil samples from the top layer within a few centimeters beneath the surface at a middle latitude location (43.06°N) (23). The CE-5 samples were collected from (i) the youngest known lunar basalts (2.0 Ga) (24–26), thus minimizing perturbations by impact cratering, and (ii) from the driest basaltic basement (7 ± 3 ppm H_2O) (27, 28), thus minimizing any possible contribution from lunar magmatic water. Therefore, CE-5 samples are key to addressing the spatial-temporal distribution and retention of the SW-derived water in the lunar regolith.

Seventeen soil grains with few adhering splashed melts were selected from two lunar soil sample fractions (*Materials and Methods*), which were scooped from the topmost layer (<3 cm in thickness) of the lunar regolith at the landing site (29). After cleaning the grain surfaces with adhesive tape to avoid using water or other liquids, the grains were pressed into indium metal mounts and then coated with gold (Fig. 1). The grains studied include seven olivine, one pyroxene, four plagioclase, and five glass, which were identified and confirmed by both the energy dispersive x-ray spectroscopy (EDS) and Raman spectra (*SI Appendix,* Fig. S1 and Table S1). The hydrogen abundances, and deuterium/hydrogen ratios were obtained from ion microprobe analysis (*Materials and Methods*). Though the ion microprobe analysis cannot discriminate the species of hydrogen, which could be present as H, H_2, OH, H_2O, and other compounds in lunar soil grains (30–33), the measured hydrogen concentrations largely reflect the amounts of the OH/H_2O and were usually expressed as "water" in previous studies (6, 13). The hydrogen isotopes were also determined to address its sources.

Results

A total of 20 depth profiles ($^1H^-$, $^2D^-$, and $^{16}O^-$ intensity versus duration of sputtering, i.e., depth) have been analyzed on the 17 grains using a nanoscale secondary ion mass spectrometer (NanoSIMS) (Fig. 2 and *SI Appendix,* Fig. S2*)* (see *Materials and Methods* for details). Since D counts in every single measurement cycle (one cycle consists of 0.54-s counting of $^1H^-$, $^2D^-$, and $^{16}O^-$ intensities) are too low to precisely determine the D/H ratio, only the bulk D/H ratio of the topmost 100 cycles (~100 nm in depth, see below) was calculated and expressed in ‰ as δD value ($\delta D\,(‰) = [(D/H)_{sample}/(D/H)_{SMOW} - 1] \times 1,000$; SMOW: standard mean ocean water) with a statistical uncertainty (1σ) derived from counting statistics (*SI Appendix,* Table S2). The depths of the NanoSIMS-sputtered craters in representative grains were measured using an atomic force microscope (AFM) (*SI Appendix,* Fig. S3), and the sputtering rate was estimated to be ~1 nm per rastering cycle (*SI Appendix,* Table S3). After the NanoSIMS analysis, ~100-nm-ultrathin slices were prepared from four of the crystals and two of the glass grains using focused ion beam (FIB), and examined using a transmission electron microscope (TEM) (Fig. 1 and *SI Appendix,* Figs. S4–S8) (*Materials and Methods*).

All the silicate crystal grains, including olivine, pyroxene, and plagioclase, show a SW-damaged zone with a thickness of 60 to 85 nm. The presence of nanophase Fe particles was observed in

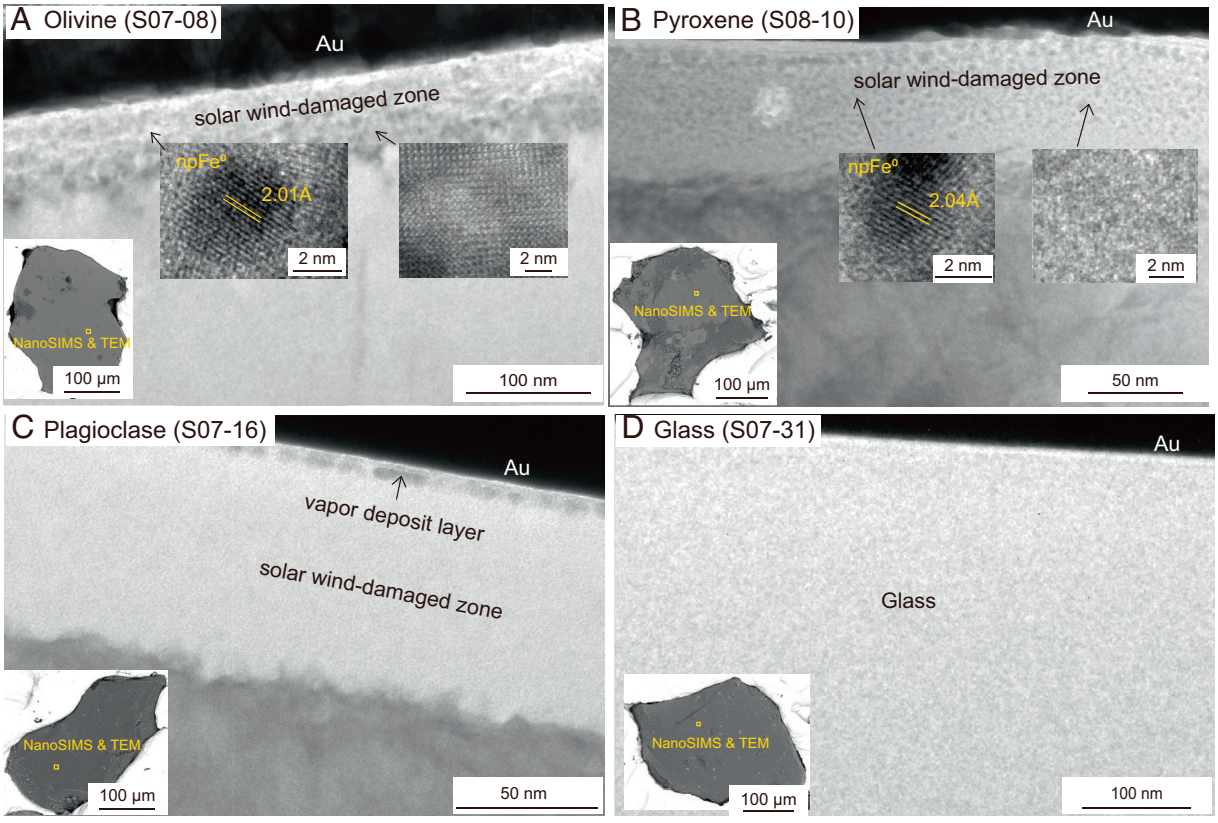

Fig. 1. Secondary electron images and TEM images of four CE-5 lunar soil grains. (*A–D*) The yellow squares marked on the grains are the areas for NanoSIMS and TEM analyses. The SW-damaged zone (60 to 85 nm in thickness) can be clearly observed in olivine, pyroxene, and plagioclase, but not in glass grain. The damaged zone is amorphous in pyroxene and plagioclase, but retains crystalline structure in olivine. Nanophase Fe ($npFe^0$) particles can be observed in the damaged zones of olivine and pyroxene. In addition, a very thin layer, probably vapor deposit, can be seen on the topmost surface of plagioclase.

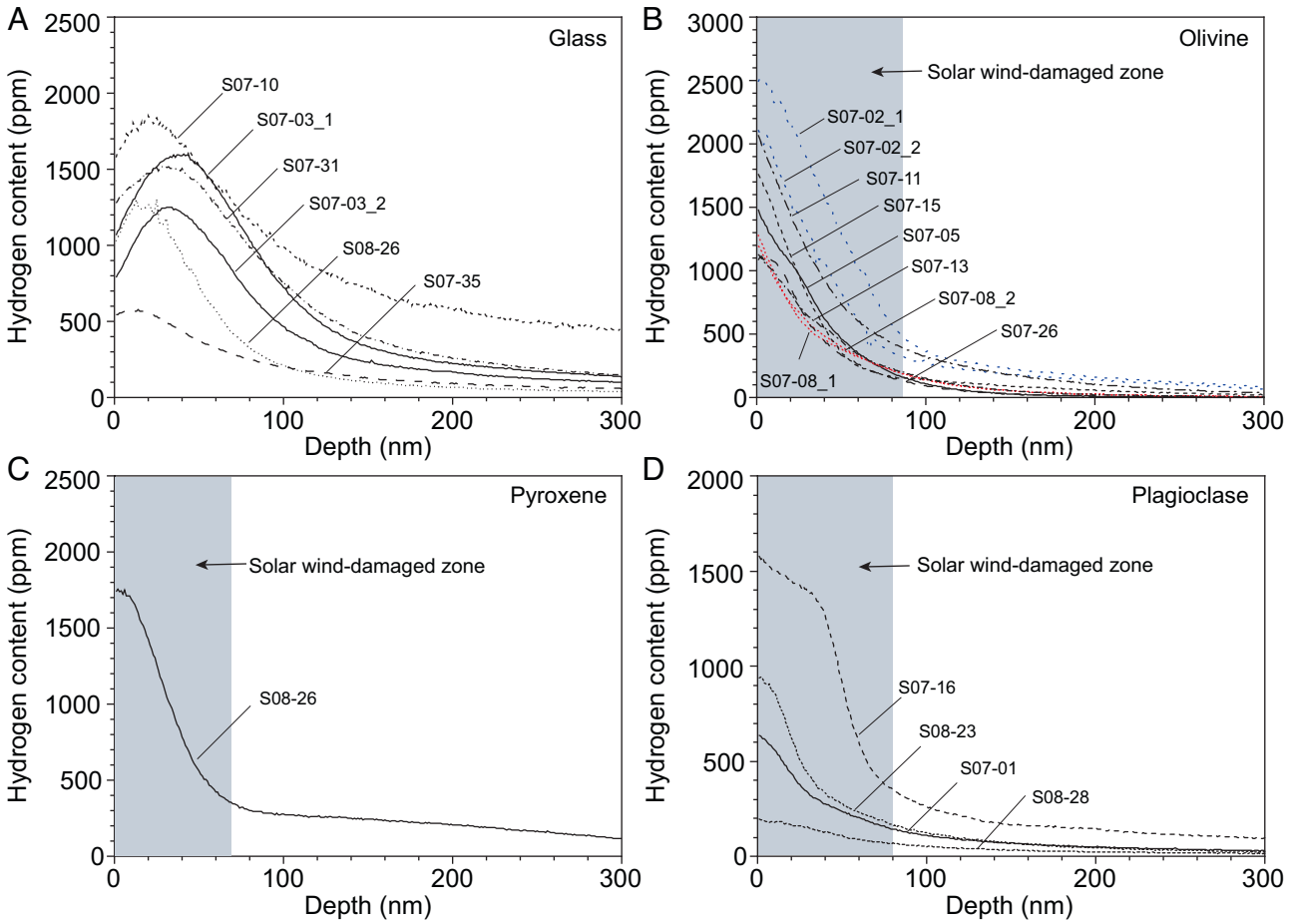

Fig. 2. The H-content depth profiles in the CE-5 soil grains. (*A–D*) Two types of H-content depth profiles were observed. The depth profiles in the glass grains show a bell-shaped distribution (*A*) with peak depths ranging from 18 to 38 nm, while those in the silicate crystals (*B–D*) display a monotonically decreasing trend. The gray areas represent the SW-damaged zone measured by TEM. Seventeen silicate grains were analyzed, including seven olivine, one pyroxene, four plagioclase, and five glass. Note that only the first 300 nm of the depth profiles are presented due to the nearly stable contents after that.

the SW-damaged zone in olivine and pyroxene but not in plagioclase (Fig. 1 *A–C* and *SI Appendix,* Figs. S4–S7). In addition, a thin (<10 nm) vapor deposit layer was observed on the topmost surface of the plagioclase grain (Fig. 1*C* and *SI Appendix,* Fig. S7). These space weathering features were not found in the glass grains (Fig. 1*D* and *SI Appendix,* Fig. S8), probably because of their amorphous nature. Solar flare tracks were recognized beneath the damaged zone of the crystalline grains (*SI Appendix,* Figs. S4–S7), as reported in Apollo lunar soil grains (34–36). The TEM-measured solar track densities of the CE-5 grains yield a range of exposure times from 0.12 Ma to 1.95 Ma (*SI Appendix,* Table S4), based on a track production rate of $4.4 \pm 0.4 \times 10^4$ tracks $cm^{-2}yr^{-1}$ for a 2π exposure at 1 AU estimated from the solar flare track density in pyroxene (36). It is important to emphasize that solar flare tracks are produced mainly by solar energetic particles, penetrating a few millimeters into the soils (36, 37). Hence the SW-irradiation time could be much shorter than the solar energetic particle exposure age because of possible shielding of the overlying grains from SW that penetrates only ~100 nm. Simply assuming a random exposure of a soil grain with a cubic form and an average size of ~50 μm within the topmost ~2-mm layer of lunar regolith (37) in a period of 0.1 to 2.0 Ma, the average SW-irradiation time was estimated to be ~410 to 8,300 y.

All the ion probe profiles show a H-enriched zone in the first <100-nm depth below the surface with hydrogen contents decreasing sharply (Fig. 2 and *SI Appendix,* Fig. S2), where the zero-depth position of the H-content depth profile was defined as the onset of steady-state sputtering at cycles 10 to 20 based on the O-count profile. The H-enriched zone in the silicate crystals overlaps the SW-damaged zone. The maximum hydrogen contents in the topmost surface zone are always high (1,116 to 2,516 ppm), except for four grains (196 to 942 ppm) (*SI Appendix,* Table S2). The H-content depth profiles are of two types (Fig. 2). All glass grains display bell-shaped H-content depth profiles with peaks at a depth of 18 to 38 nm (average of 26 ± 7 nm) (Fig. 2*A* and *SI Appendix,* Table S2). In contrast, the silicate crystals exhibit a monotonically decreasing trend without any peak, except for one plagioclase grain (S07-16) showing a inflection point (Fig. 2 *B–D*). The topmost ~100-nm H-enriched zone of the grains is always highly D-depleted, with the bulk δD values ranging from −908 ± 12‰ to −992 ± 6‰, except for three grains, which are slightly less D-depleted (one glass grain probably resulting from impact melting of lunar soil because of the significant presence of hydrogen, ~210 ppm at depth of 900 nm; two plagioclase grains with low hydrogen contents of 196 and 637 ppm in the topmost surface zone) (*SI Appendix,* Table S2).

The extremely low δD values of the topmost ~100-nm zone in both the silicate crystals and glass grains imply that the hydrogen present in CE-5 grains is nearly exclusively of SW origin. In fact, the D-depletion is a fingerprint of SW-H because the Sun is devoid of deuterium due to nuclear burning in the protosun (38). This signature is clearly different from the δD values of chondrites

(−230 to +1,000‰) (39, 40), comets (−100 to +3,175‰) (39, 41), and the lunar interior reservoir (0 ± 200‰) (42–44). It is worth noting that the vapor deposit contributes little, if anything, to the δD values, as indicated by the fact that the same bulk δD values are obtained for the topmost 100-nm zone, whether or not excluding the first 10 nm (*SI Appendix*, Table S2). The consistent lowest δD values of −990 to −992‰ observed for five grains are identical to the present-day SW collected by the Genesis mission (<−997‰) (45), indicating a nearly pure SW component in these grains. This can probably be related to the low endogenic water in the host basalts (27): there is essentially no contribution of hydrogen from a source other than the SW. These implanted SW-H could be trapped in the defect sites or by forming new molecular species with lattice atoms (30), and H_2 molecules are likely formed when the concentrations of unreacted H atoms are high (32). Based on the average hydrogen contents of the topmost 100-nm zone in the CE-5 soil grains and the grain size distribution as Apollo soils (*Materials and Methods*), the bulk abundance of SW-derived water (assuming hydrogen all as water) of the CE-5 soils was estimated at ~46 ppm, consistent with the remote sensing measurements at CE-5 landing site (15, 46). This estimated value could be regarded as an upper limit, since the implanted SW-H is usually considered not to be all bonded with O in the lunar soils (11, 47).

Discussion

Note that the CE-5 soil grains were in fact not from the very surface of the lunar regolith but have been buried, since the topmost dust has been blown off by the lander exhaust. The relatively constant maximum hydrogen contents (1,116 to 2,516 ppm) in the topmost ~100-nm zone of the soil grains reveal an efficient preservation of the SW-derived hydrogen after burial. This is supported by the heating experiments that we performed on a subset of the CE-5 soil grains at a higher temperature (~450 K) than the noon temperature at the CE-5 landing site (*Materials and Methods*). The heating experiments are used to estimate the possible maximum loss of hydrogen and the diffusion rate of hydrogen in the SW-damaged zone. The H-content depth profiles in the heated grains still kept their original types. In addition, the maximum hydrogen contents in the grain rims were reduced by less than 20% after heating at 450 K for 28 h, except for one grain with a H-content reduction of ~40% (Fig. 3 *A* and *B* and *SI Appendix*, Table S5). However, this significant reduction could

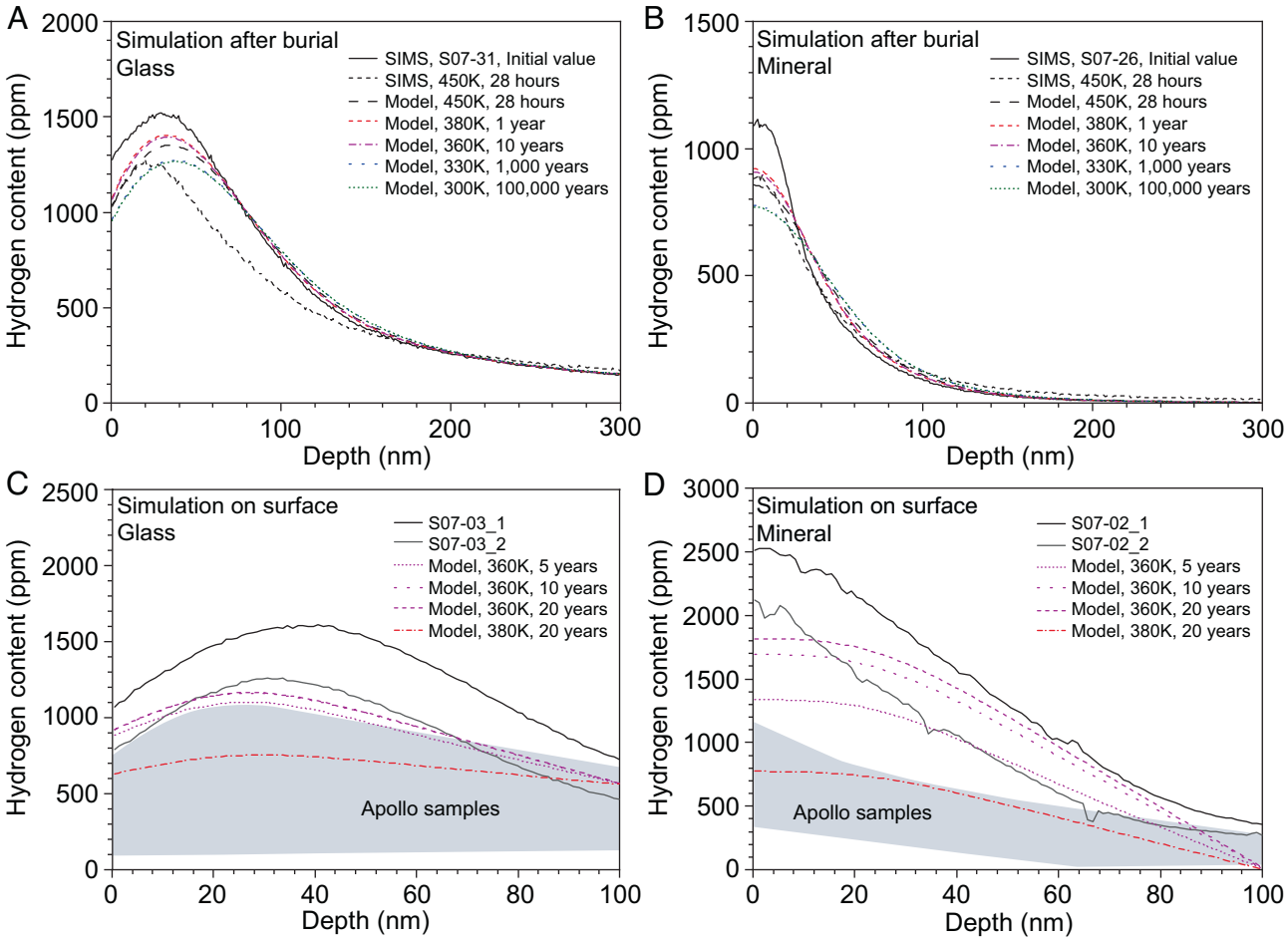

Fig. 3. Simulation results of the H-content depth profiles in glass and silicate crystal grains. (*A* and *B*) Simulations of diffusion after burial. The changes in H-content depth profiles during heating experiments on one glass (S07-31) and one olivine (S07-26) were taken to compare with the computing simulation results. The heated grains show a systematic decrease in their maximum hydrogen contents in the surface zone (with a slight variability in glass S07-31) and a flattening of the profile inward, e.g., hydrogen contents are higher than initial in the interior for olivine S07-26 (38 ppm vs. <2 ppm at 300 nm depth). (*C* and *D*) Computing simulation of dynamic equilibrium on the surface. The dynamical equilibrium of implantation and diffusion in glass and minerals were calculated for a maximum temperature of 360 K (at the CE-5 landing site) and compared with the H-content depth profiles for one glass (S07-03) and one olivine (S07-02). The maximum hydrogen contents in the surface zone of the depth profiles could be achieved within 10 to 20 y of SW-H implantation. The simulation for a higher temperature of 380 K was taken to compare with the Apollo samples (gray areas) measured by SIMS (50, 51) and NRA $^{1}H(^{19}F, \alpha\gamma)^{16}O$ technique (52, 53).

be at least partially attributed to the heterogeneous hydrogen distribution in the grains as indicated by the duplicated analyses on three of the grains (Fig. 2 *A* and *B* and *SI Appendix*, Table S2). The heating results demonstrate the high stability of the SW-implanted hydrogen in the soil grains. Therefore, the distribution of SW-derived hydrogen in the CE-5 lunar grains was mainly established during the dynamic equilibrium processes between implantation and outgassing of SW-H on the topmost surface of the Moon. The diffusion loss of hydrogen after burial to a few centimeter depth is minor. Modeling of the heating experiments (Fig. 3 *A* and *B*) results in a diffusion rate of ~3×10^{-17} cm^2/s at 450 K with a high activation energy of 1.3 eV in the SW-damaged rims of the CE-5 soil grains. Because the species of hydrogen cannot be known in the ion microprobe analysis, the calculated diffusion rates through modeling the heating experiments actually refer to the average value of different H species. This high activation energy is similar to the value estimated for hindered diffusion in irradiated silica (48). With these parameter constraints, it was found that the observed H-content depth profiles of the CE-5 grains can be preserved for 10 to 10^5 y after burial to a few centimeters below the surface (Fig. 3 *A* and *B* and *SI Appendix*, Table S6), where the maximum temperature is in the range of 360 to 300 K (49). By contrast, the Apollo soils, situated at a higher temperature by ~20 K relative to the CE-5 soils, could have experienced significant diffusion loss of the SW-derived hydrogen, whereas the soils in the polar regions (~300 K at a latitude of 75°) could be almost completely preserved from diffusion loss.

Thus, the observed H-content depth distributions in the CE-5 soil grains have preserved the results of the on-going surficial processes before burial. In agreement with the SW-origin, the bell-shaped H-content depth profiles in the glass grains peak at the same depth (26 ± 7 nm) as the one simulated for the implantation of 1 keV H^+ (peak at ~22 nm in depth) (20) and the SW-H-implanted curves recorded in the Genesis collectors (45). At variance with the glass grains, the silicate crystals exhibit a monotonically decreasing distribution of hydrogen with depth (Fig. 2 *B*–*D*). The heated grains display the same types of depth profiles as the preheating ones, supporting that the H-content peak observed in the glass grains would not be the result of simple hydrogen diffusion after burial. Thus, simulations were conducted to explore whether the observed two types of hydrogen depth distributions could be produced when considering the dynamic processes that affect SW-H in soil grains exposed on the lunar surface (*Materials and Methods*). The SW-H dynamic equilibrium processes involve implantation and diffusion in the SW-damaged zone, and outgassing from the grain surface. The implanted hydrogen depth distributions were assumed to be nearly the same for all silicate phases with a theoretical SW-H implantation peak depth of ~22 nm (depending on the energy of SW-H). Based on the observed depth distribution, the simulations reveal that the formation of these two types of H-content depth profiles requires different outgassing rates of SW-H from the grain surface between silicate crystals and glass. One scenario is that some mechanism inhibits the outgassing of H from the surface of silicate crystals relative to glass, resulting in the accumulation of SW-H just beneath the crystal surface, which likely leads to the disappearance of the H peak (Fig. 3 *C* and *D*). Further studies will try to unveil the nature of this mechanism. Furthermore, the simulations show that the observed two types of H-content depth distributions, with maximum hydrogen contents (1,116 to 2,516 ppm) in the rims of the grains, could be achieved within 10 to 20 y of SW-H implantation. This minimum equilibrium exposure time is much shorter than the aforementioned SW-irradiation time (~410 to 8,300 y), suggesting that some saturation level of the SW-derived hydrogen in the lunar soil grains was reached rapidly. This is also supported by the relatively constant maximum hydrogen contents (1,116 to 2,516 ppm) in the topmost surface zone of the CE-5 grains.

The parameters used to model the SW-H dynamic equilibrium between implantation, diffusion, and outgassing in the grains were constrained by the H-content depth profiles observed for the CE-5 soil grains (maximum temperature of ~360 K at the landing site) and those for the Apollo returned samples (maximum temperature of ~380 K at the Apollo 11 landing site) (Fig. 3 *C* and *D* and *Materials and Methods*). The H-content depth profiles of Apollo samples were previously analyzed, several grains by resonant nuclear reaction (NRA) $^1H(^{19}F, \alpha\gamma)^{16}O$ technique (52, 53), one Apollo-17 silicate grain (79035) by SIMS (50), and nine Apollo 11 soil grains by NanoSIMS (51). Similarly to SIMS, NRA cannot discriminate the species of hydrogen. The maximum H-contents in the topmost surface zone of the Apollo grains measured by both SIMS and NRA are systematically lower than the values of the CE-5 soil grains (Fig. 4). Furthermore, the dynamic equilibrium model, established by fitting the H-content depth profiles in CE-5 and Apollo soil grains, is used to predict the H-content in lunar soil in the polar region. The model predicts very high maximum H-contents in the topmost ~100-nm zone of soil grains in the lunar polar regions, where the maximum temperature is only ~300 K, up to ~15,000 ppm for glass and ~38,900 ppm for silicate crystals, respectively (*SI Appendix*, Fig. S9). These predicted maximum H-contents in silicate crystals appear too high, nearly requiring every O to be bonded to a H. Conservatively, the predicted hydrogen depth distribution in the topmost surface zone of glass was used to estimate the bulk abundance of SW-derived water in lunar polar regions. Based on the predicted H-content depth profile in *SI Appendix*, Fig. S9*A*, the calculated average of the H content in the topmost 100-nm zone of the glass is ~9,500 ppm. Taking this predicted value, the water abundance of the bulk soil in the polar regions is estimated to be ~560 ppm, assuming the same grain size distribution as Apollo soils. This water content is consistent with the orbit remote sensing analysis in the polar region (~400 to 700 ppm) (15). Therefore, the discoveries of the CE-5 lunar soil grains shed light on the dynamic equilibrium between the implantation and outgassing of SW-derived hydrogen on the topmost surface of the Moon and subsequently diffusion loss of the hydrogen after burial, and provide significant constraints on the temperature (hence latitude) effects on these processes.

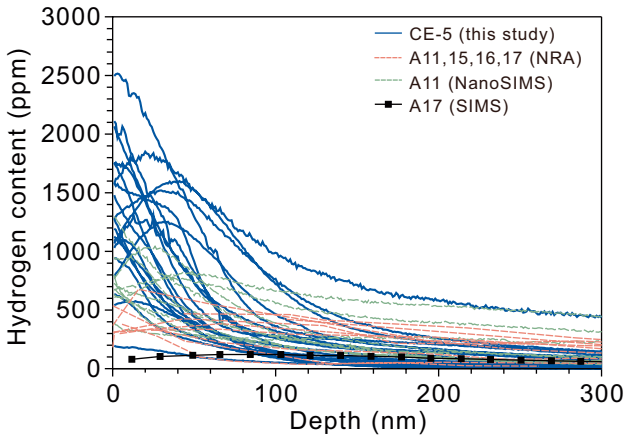

Fig. 4. Distribution of hydrogen in CE-5 lunar soil grains compared with Apollo samples. The Apollo data obtained from both the NRA and SIMS techniques (50–53) are shown.

Materials and Methods

Sample Preparations. Two CE-5 lunar soil sample fractions (CE5C0400YJFM00409, ~500 mg; CE5C0400YJFM00407, ~1,000 mg) studied in this work were allocated by the China National Space Administration. Both of them were scooped from the lunar surface. The samples were stored in the gloveboxes filled with high-purity nitrogen installed at the Institute of Geology and Geophysics, Chinese Academy of Sciences (IGGCAS). Various mineral phases including olivine, pyroxene, plagioclase, and glass were hand-picked in an ultraclean lab. The adhesive tape was used to clean most adhered materials on the surface, and then the grains were directly pressed into two high-purity indium mounts labeled as "S07" and "S08". During sample preparations, the soil grains have been exposed to the air for a short time. San Carlos olivine grains with low water content (H_2O = 1.4 ppm) (54) were also pressed into the indium mounts without polishing. The sample mounts were kept in a vacuum box until they were analyzed. The possible H surface contamination is negligible, as shown by monitoring the San Carlos olivine (*SI Appendix*, Fig. S11 *E* and *F*).

Scanning Electron Microscope (SEM) Analysis. The sample mounts were coated with ~10-nm-thick Au for the SEM analysis. The surface features of individual grains were observed with a Thermo scientific Apreo S instrument installed at the IGGCAS, using an acceleration voltage of 15 kV and electron beam current of 6.4 nA. In addition, a Zeiss Auriga Compact dual beam instrument equipped with an EDS was used to identify the mineral phases and determine the compositions (*SI Appendix*, Table S1).

In Situ NanoSIMS Analysis. After SEM analysis, the sample mounts were recoated with Au (~50 nm thick) in order to acquire as much as possible intact H-content depth profiles and to insure good surface conductivity. The analyses were carried out with a CAMECA NanoSIMS 50L at the IGGCAS. The sample mounts with the CE-5 grains and the standards were first loaded in the airlock, baked overnight at ~60°. Then, the sample mounts were stored in the sample chamber for 7 d to improve the vacuum quality and minimize the background H. The vacuum in the analysis chamber was ~3×10^{-10} Torr during analysis. The area of 7 × 7 μm^2 was rastered using a Cs^+ beam of ~500 pA current with a beam diameter of 0.8 to 1 μm. The outer 71.8% of the rastered areas was blanked off in order to further reduce background values using the electronic gate technique. The multicollection isotope mode was used to count the secondary ions $^1H^-$, $^2D^-$ by electron multipliers and $^{16}O^-$ by a Faraday cup. An electron-gun was applied for sample surface charge compensation. The counting time is 0.54 s per cycle, and each depth profile contains a total of 1,000 to 2,500 cycles. The depths of the ion probe-sputtered craters were determined by an AFM, and the sputtering rate was calculated to be ~1 nm per cycle (*SI Appendix*, Table S3).

San Carlos olivine grains were pressed in the same indium mounts with the lunar grains, and used as the reference for monitoring H background and possible surface contamination (*SI Appendix*, Fig. S10). The transient sputtering effects produced during the depth-profiling measurement have been considered (55). The oxygen intensity increases from the beginning of the sputtering and then reaches a steady state. Based on the depth profiles, the 90% of the average stable oxygen counts were chosen as the start position of the depth profile to eliminate the transient sputtering period at the beginning of the measurements (*SI Appendix*, Fig. S11). The determined start position is referred to as the zero depth shown in Fig. 2 and *SI Appendix*, Fig. S2. It is evident that the presence or lack of a peak in the H-content depth profiles in the grains is not an analytical artifact due to the choice of the zero-depth position (*SI Appendix*, Fig. S11). In addition, only the first 300 nm of the depth profiles are presented in these figures, due to the nearly stable hydrogen contents after that. Then, the H-count depth profiles of the grains were calculated by subtracting the H counts of San Carlos olivine to account for residual background hydrogen on the sample. The H counts on the surface of San Carlos olivine is less than 2% of that of the soil grains. The H contents of the CE-5 soil grains were one-ninth of their water contents, which were calculated from the background-subtracted H/O ratios multiplied by the slope of the calibration line (*SI Appendix*, Fig. S12). The calibration line was determined from measuring the standards Kovdor apatite (H_2O = 0.98 ± 0.07 wt%, δD = −66 ± 21‰) (56), Durango apatite (H_2O = 0.0478 wt%, δD = −120 ± 5‰) (5), SWIFT MORB glass (H_2O = 0.258 wt%, δD = −73 ± 2‰), and the San Carlos olivine (H_2O = 1.4 ppm) (54). Corrections for instrumental mass fractionation (IMF) on H isotopic compositions of samples were conducted on the Kovdor apatite standard using $\alpha_{IMF} = (D/H)_{measured} / (D/H)_{recommended}$. The α_{IMF} of the standards is 1.09, and the variation in α_{IMF} is ~50‰ (2σ). Since D counts of lunar soils in every single cycle are too low to determine the D/H ratio, only the bulk D/H ratio of the topmost 100 cycles (~100 nm) was calculated and expressed in ‰ as δD value: $\delta D\ (‰) = [(D/H)_{sample} / (D/H)_{SMOW} - 1] \times 1,000$, where SMOW is the standard mean ocean water with a D/H ratio of 1.5576×10^{-4}. The δD values are reported with 1σ, which is derived from counting statistics.

Raman Analysis. The Raman spectrum was collected using a confocal Raman microscope alpha 300R made by WITec GmbH (Ulm, Germany) at the IGGCAS. This system is equipped with a solid-state continuous-wave laser emitting at 532 nm, which is fiber coupled to the instrument. A laser power of about ~7 mW was focused on the sample surface (57). A piece of single-crystal silicon was used to calibrate the wavenumbers of the shifts. The Raman spectra from 200 to 1,600 cm^{-1} were taken, and the integrating time was ~4 min. Different mineralogy phases were identified by their diagnostic spectra (*SI Appendix*, Fig. S1).

Depth Measurements Using AFM. An AFM (Bruker Corp., Dimension Icon) installed in an Ar-filled glovebox (H_2O concentration < 1 ppm, O_2 concentration < 1 ppm) was utilized to measure the NanoSIMS crater depths. The topography of the nine representative grains was acquired using a silicon AFM probe (k = 26 N/m, f_0 = 300 kHz) with a scan rate of 0.854 Hz (about 5 min for each analysis) under the peakforce quantitative nanomechanical mode (58).

As the grain surfaces are usually not perfectly flat, we first used a detrending technique to obtain a horizontal background surface. This was done by fitting the original surface with a plane and then subtracting the elevation of this fitting plane from the original surface to have a background elevation of about zero (*SI Appendix*, Fig. S3). A crater depth was analyzed using 10 lines (5 North–South and 5 West–East) across the crater to get an average. Three grains of each mineral phase were averaged to get the sputtering rate (*SI Appendix*, Table S3). Then, the peak position of the glass grains was calculated by rejecting the sputtering cycles based on the 90% of the stable oxygen counts, and multiplying the sputtering depth per rastered cycle and cycle number.

Transmission Electron Microscopy Analysis. The microstructure characteristics were observed on six representative grains. The areas analyzed in NanoSIMS measurements were cut and picked up using the FIB. The FIB operation was conducted with a Zeiss Auriga Compact dual beam instrument equipped with an Omniprobe AutoProbe 200 micromanipulator at the IGGCAS. Ion beam conditions for the final thinning and polishing were 5 to 30-kV high voltage with beam currents of 50 pA to 2 nA. Each FIB section was prepared to ~100 nm in thickness. Then, the ultrathin specimens were analyzed by a TEM (JEOL JEM-2100), operating at the voltage of 200 kV. Phase structures were analyzed by high-resolution TEM imaging, and the chemical compositions of the samples were obtained by EDS elemental spot analysis.

The exposure age of the lunar grains was determined by counting solar flare tracks in the TEM images, which were imported into CorelDRAW software for drawing and counting. The track density was calculated by dividing the number of tracks with the counted image area. The solar flare tracks were counted within the topmost zone of 0.5 μm, and the track production rate of $4.4 \pm 0.4 \times 10^4$ tracks $cm^{-2}yr^{-1}$ at 1 AU (36) was used to determine the exposure age of each grain (*SI Appendix*, Figs. S4–S7 and Table S4).

Heating-Diffusion Experiments. After the ion probe analyses of hydrogen contents and D/H isotopic ratios of the CE-5 lunar soil grains, one of the olivine grains (S07-26) and two of the glass grains (S07-10 and S07-31) were selected for heating-diffusion experiments (*SI Appendix*, Table S5). They were picked out from the original sample mount, and heated at ~450 K for 28 h in a drying oven. The heated grains were then pressed into a new high-purity indium mount. The H-content depth profiles were conducted on these heated grains with the NanoSIMS following the method depicted above.

Simulations of the SW-H Implantation and Diffusion. On the basis of the heating experiments on glass (S07-31) and olivine (S07-26) grains, the heated H-content depth profiles were fitted to establish the diffusion outgassing of hydrogen after burial of the CE-5 soil grains. The distribution of hydrogen was modeled following Fick's law in one dimension, and the numerical solution to the partial differential equations was solved with finite-difference equivalent. The H-content depth profile measured before heating experiment was the initial concentration gradient. The diffusion coefficient was determined following $D = D_0 e^{(-\frac{U}{T})}$, where

T = 450 K, in which a pre-exponential factor of $D_0 = 10^{-6}$ m^2/s (20, 59) and a high activation energy of diffusion $U = 1.3$ eV (60) were found by fitting the heated value. In addition, some constraints for the possible surface process were required to reproduce the heating results, e.g., chemisorbed H-atoms breaking O–H bonds to form hydrogen molecules (60). This recombination-limited outgassing rate of hydrogen was expressed as a flux following $q = Kn_H . n_H$, where n_H is the concentration of implanted H at the surface boundary and K is the effective chemical constant, which follows the similar Arrhenius equations relating with diffusion coefficient. Though the details of recombination-limited outgassing were poorly understood, different pre-exponential factors for mineral (0.0001) and glass (0.01) were found to fit the data well. The retention of hydrogen in the lunar soils after burial are predicted in *SI Appendix*, Table S6.

The retention of the SW-derived hydrogen in surface soils was mainly established by dynamic equilibrium between SW-H implantation and diffusion. The implanted-SW flux was estimated with $n_{sw}v_{sw}\cos(Z)$, where $n_{sw} = 5 \times 10^6$ atoms/m^3, $v_{sw} = 4 \times 10^5$ m/s, and Z are the SW density, velocity, and incidence angle, respectively (61). The implanted protons were assumed to follow a Gaussian distribution, where the typical depth of 22 nm and spatial widths of 13 nm are set as suggested by Transport in Ion Material (TRIM) results for 1-keV protons (20). As mentioned above, the diffusion also followed the Fick's law. The highest surface temperature is estimated with $T = 280\ cos^{0.25}(Z) + 100$ K (62), where T ~360 K at CE-5 landing site and ~20 K higher at Apollo landing sites. The parameters in the simulation modeling of dynamic equilibrium between SW-H implantation and diffusion performed by Farrell et al. (61) were taken to simulate the experimental data (Fig. 3 *C* and *D*). Moreover, the simulations of dynamic equilibrium were made by following the same calculation to predict the hydrogen contents in the soil grains at the latitude of 0° and 75° with the T of 380 K and 300 K, respectively (*SI Appendix*, Fig. S9).

Water Contents Estimated for Bulk Lunar Soils. Based on the H-content depth profiles of the soil grains, the SW-derived hydrogen is predominantly concentrated in the outmost zone of the grain rims (<100 nm in thickness). Assuming all implanted SW-H bonded with O in the lunar soils, the average concentration of SW-derived water in the outmost 100-nm zone of the CE-5 grains is ~7,000 ppm based on all 20 depth profiles; and that of the polar soil grains is ~85,500 ppm based on the predicted H-content depth profile of glass at the high latitude. Taking the same grain size distribution of the Apollo lunar soils (the second solid line plotted in figure 11 in ref. 63), the bulk SW-derived water contents were estimated ~46 ppm for the CE-5 lunar soils and ~560 ppm for the soils at high latitude.

Data, Materials, and Software Availability. All study data are included in the article and/or *SI Appendix*. We also deposited the data in Figshare (https://figshare.com/articles/dataset/High_abundance_of_solar_wind-derived_water_in_lunar_soils_from_the_middle_latitude/21607740)

ACKNOWLEDGMENTS. We are grateful to the constructive reviews by two anonymous reviewers. We thank the China National Space Administration (CNSA) for providing the CE-5 lunar samples. We also thank Xiaoguang Li for Raman analysis, Xu Tang for TEM analysis, and Jing Wan and Huijuan Yan for AFM analysis. This study was funded by the National Natural Science Foundation of China (41973064, 42103035, and 42230206), the Key Research program of Chinese Academy of Sciences (QYZDJ-SSW-DQC001, ZDBS-SSW-JSC007), the Preresearch project on Civil Aerospace Technologies by CNSA (D020201, D020203), and the key research program of the Institute of Geology and Geophysics, Chinese Academy of Sciences (IGGCAS-202101).

Author affiliations: [a]State Key Laboratory of Space Weather, National Space Science Center, Chinese Academy of Sciences, Beijing 100190, China; [b]Key Laboratory of Earth and Planetary Physics, Institute of Geology and Geophysics, Chinese Academy of Sciences, Beijing 100029, China; [c]Institut de Physique du Globe de Paris, Université de Paris, CNRS, Paris 75005, France; and [d]State Key Laboratory of Lithospheric Evolution, Institute of Geology and Geophysics, Chinese Academy of Sciences, Beijing 100029, China

1. G. H. Heiken, D. T. Vaniman, B. M. French, *Lunar Sourcebook, A User's Guide to the Moon* (Cambridge University Press, Cambridge, 1991).
2. Y. G. Shkuratov, N. V. Bondarenko, Regolith layer thickness mapping of the Moon by radar and optical data. *Icarus* **149**, 329–338 (2001).
3. J. Zhang *et al.*, Lunar regolith and substructure at Chang'E-4 landing site in South Pole-Aitken basin. *Nat. Astro.* **5**, 25–30 (2021).
4. D. S. McKay *et al.*, The lunar regolith. *Lunar Sourcebook* **567**, 285–356 (1991).
5. J. P. Greenwood *et al.*, Hydrogen isotope ratios in lunar rocks indicate delivery of cometary water to the Moon. *Nat. Geosci.* **4**, 79–82 (2011).
6. Y. Liu *et al.*, Direct measurement of hydroxyl in the lunar regolith and the origin of lunar surface water. *Nat. Geosci.* **5**, 779–782 (2012).
7. A. E. Saal *et al.*, Volatile content of lunar volcanic glasses and the presence of water in the Moon's interior. *Nature* **454**, 192–195 (2008).
8. F. M. McCubbin *et al.*, Nominally hydrous magmatism on the Moon. *Proc. Natl. Acad. Sci. U.S.A.* **107**, 11223–11228 (2010).
9. R. Tartèse *et al.*, The abundance, distribution, and isotopic composition of Hydrogen in the Moon as revealed by basaltic lunar samples: Implications for the volatile inventory of the Moon. *Geochim. Cosmochim. Acta* **122**, 58–74 (2013).
10. S. Epstein, H. P. Taylor Jr., The concentration and isotopic composition of hydrogen, carbon and silicon in Apollo 11 lunar rocks and minerals. *Geochim. Cosmochim. Acta* **1**, 1085–1096 (1970).
11. S. Epstein, H. P. Taylor Jr., "The isotopic composition and concentration of water, hydrogen, and carbon in some Apollo 15 and 16 soils and in the Apollo 17 orange soil" in *Proc. 4th Lunar Sci. Conf.* (Lunar Science Institute, 1973), vol. **4**, p. 1559.
12. I. Friedman *et al.*, Water, hydrogen, deuterium, carbon, carbon-13, and oxygen-18 content of selected lunar material. *Science* **167**, 538–540 (1970).
13. A. Stephant, F. Robert, The negligible chondritic contribution in the lunar soils water. *Proc. Natl. Acad. Sci. U.S.A.* **111**, 15007–15012 (2014).
14. C. M. Pieters *et al.*, Character and spatial distribution of OH/H_2O on the surface of the Moon seen by M^3 on Chandrayaan-1. *Science* **326**, 568–572 (2009).
15. S. Li, R. Milliken, Water on the surface of the Moon as seen by the Moon Mineralogy Mapper: Distribution, abundance, and origins. *Sci. Adv.* **3**, e1701471. (2017).
16. C. Wöhler *et al.*, Time-of-day-dependent global distribution of lunar surficial water/hydroxyl. *Sci. Adv.* **3**, e1701286 (2017).
17. W. C. Feldman *et al.*, Fluxes of fast and epithermal neutrons from lunar prospector: Evidence for water ice at the lunar poles. *Science* **281**, 1496–1500 (1998).
18. R. N. Clark, Detection of adsorbed water and hydroxyl on the Moon. *Science* **326**, 562–564 (2009).
19. J. M. Sunshine *et al.*, Temporal and spatial variability of lunar hydration as observed by the Deep Impact spacecraft. *Science* **326**, 565–568 (2009).
20. W. M. Farrell, D. M. Hurley, M. I. Zimmerman, Solar wind implantation into lunar regolith: Hydrogen retention in a surface with defects. *Icarus* **255**, 116–126 (2015).
21. O. J. Tucker *et al.*, Solar wind implantation into the lunar regolith: Monte Carlo simulations of H retention in a surface with defects and the H_2 exosphere. *J. Geophys. Res.* **124**, 278–293 (2019).
22. X. Zeng *et al.*, Experimental investigation of OH/H_2O in H^+-irradiated plagioclase: Implications for the thermal stability of water on the lunar surface. *Earth Planet. Sci. Lett.* **560**, 116806 (2021).
23. W. Yang, Y. Lin, New lunar samples returned by Chang'e-5: Opportunities for new discoveries and international collaboration. *Innov. (N Y)* **2**, 100070 (2020).
24. L. E. Borg, C. K. Shearer, Y. Asmerom, J. J. Papike, Prolonged KREEP magmatism on the Moon indicated by the youngest dated lunar igneous rock. *Nature* **432**, 209–211 (2004).
25. X. Che *et al.*, Age and composition of young basalts on the Moon, measured from samples returned by Chang'e-5. *Science* **374**, 887–890 (2021).
26. Q. L. Li *et al.*, Two billion-year-old volcanism on the Moon from Chang'E-5 basalts. *Nature* **600**, 54–58 (2021).
27. S. Hu *et al.*, A dry lunar mantle reservoir for young mare basalts of Chang'E-5. *Nature* **600**, 49–53 (2021).
28. F. M. McCubbin *et al.*, Magmatic volatiles (H, C, N, F, S, Cl) in the lunar mantle, crust, and regolith: Abundances, distributions, processes, and reservoirs. *Am. Min.* **100**, 1668–1707 (2015).
29. C. Li *et al.*, Characteristics of the lunar samples returned by Chang'E-5 mission. *Natl. Sci. Rev.* **9**, nwab1188 (2022).
30. J. P. Bibring, Y. Langevin, F. Roccard, Synthesis of molecules by irradiation in silicates. *J. Geophys. Res.* **87**, A446–A450 (1982).
31. A. S. Ichimura, A. P. Zent, R. C. Quinn, M. R. Sanchez, L. A. Taylor, Hydroxyl (OH) production on airless planetary bodies: Evidence from H^+/D^+ ion-beam experiments. *Earth Planet. Sci. Lett.* **345**, 90–94 (2012).
32. L. Nuccio, S. Agnello, R. Boscaino, Intrinsic generation of OH groups in dry silicon oxide upon thermal treatments. *Appl. Phys. Lett.* **93**, 151906 (2008).
33. M. J. Schaible, R. A. Baragiola, Hydrogen implantation in silicates: The role of solar wind in SiOH bond formation on the surfaces of airless bodies in space. *J. Geophys. Res. Plantes* **119**, 2017–2028 (2014).
34. L. P. Keller, D. S. McKay, Discovery of vapor deposits in the lunar regolith. *Science* **261**, 1305–1307 (1993).
35. L. P. Keller, D. S. McKay, The nature and origin of rims on lunar soil grains. *Geochim. Cosmochim. Acta* **61**, 2331–2341 (1997).
36. L. P. Keller *et al.*, Solar energetic particle tracks in lunar samples: A transmission electron microscope calibration and implications for lunar space weathering. *Meteorit. Planet. Sci.* **56**, 1685–1707 (2021).
37. S. Dust, G. Crozaz, "68815 revisited" in *Proc. 8th Lunar Sci. Conf.* (Lunar Science Institute, 1977), pp. 2315–2319.
38. D. D. Clayton, *Principles of stellar evolution and nucleosynthesis* (Univ. of Chicago Press, 1983).
39. C. M. O. D. Alexander *et al.*, The provenances of asteroids, and their contributions to the volatile inventories of the terrestrial planets. *Science* **337**, 721–723 (2012).
40. F. Robert, The D/H ratio in chondrites. *Space Sci. Rev.* **106**, 87–101 (2003).
41. D. Bockelée-Morvan *et al.*, Deuterated water in Comet C/1996 B2 (Hyakutake) and its implications for the origin of comets. *Icarus* **133**, 147–162 (1998).
42. A. Stephant *et al.*, The hydrogen isotopic composition of lunar melt inclusions: An interplay of complex magmatic and secondary processes. *Space Sci. Rev.* **284**, 196–221 (2020).
43. J. J. Barnes *et al.*, The origin of water in the primitive Moon as revealed by the lunar highlands samples. *Earth Planet. Sci. Lett.* **390**, 244–252 (2014).
44. E. H. Hauri, A. E. Saal, M. J. Rutherford, J. A. Van Orman, Water in the Moon's interior: Truth and consequences. *Earth Planet. Sci. Lett.* **409**, 252–264 (2015).

45. G. Huss, "A new upper limit on the D/H ratio in the solar wind" in *43rd Lunar Planet. Sci. Conf.* (Lunar Science Institute, 2012), p. 1709.
46. H. Lin *et al.*, In situ detection of water on the Moon by the Chang'E-5 lander. *Sci. Adv.* **8**, eabl9174 (2022).
47. L. Daly *et al.*, Solar wind contributions to Earth's oceans. *Nature Astronomy* **5**, 1275–1285 (2021).
48. D. Fink *et al.*, Hydrogen implantation and diffusion in silicon and silicon dioxide. *Appl. Phys. A* **61**, 381–388 (1995).
49. Z. Zhong, J. Yan, Z. Xiao, Lunar regolith temperature variation in the Rümker region based on the real-time illumination. *Remote Sensing* **12**, 731 (2020).
50. K. Hashizume *et al.*, Solar wind record on the Moon: Deciphering presolar from planetary nitrogen. *Science* **290**, 1142–1145 (2000).
51. H. Tian *et al.*, Solar wind-implanted water in Apollo 11 lunar soils and its implications. *Acta Petrol. Sin.* **6**, 1823–1831 (2022).
52. D. A. Leich, "The depth distribution of hydrogen and fluorine in lunar samples" in *Proc. 4th Lunar Sci. Conf.* (Lunar Science Institute, 1973), vol. **4**, pp. 1597–1612.
53. D. A. Leich, T. A. Tombrello, D. S. Burnett, The depth distribution of hydrogen in lunar materials. *Earth Planet. Sci. Lett.* **19**, 305–314 (1973).
54. W. F. Zhang *et al.*, Optimization of SIMS analytical parameters for water content measurement of olivine. *Surf. Interface Anal.* **52**, 224–233 (2020).
55. G. R. Huss *et al.*, Hydrogen fluence in Genesis collectors: Implications for acceleration of solar wind and for solar metallicity. *Meteorit. Planet. Sci.* **55**, 326–351 (2020).
56. S. L. Nadeau, S. Epstein, E. Stolper, Hydrogen and carbon abundances and isotopic ratios in apatite from alkaline intrusive complexes, with a focus on carbonatites. *Geochim. Cosmochim. Acta* **63**, 1837–1851 (1999).
57. J. Gao *et al.*, Raman and infrared spectra to monitor the phase transition of natural kyanite under static compression. *J. Raman Spectrosc.* **51**, 2102–2111 (2020).
58. J. Wan *et al.*, Ultra-thin solid electrolyte interphase evolution and wrinkling processes in molybdenum disulfide-based lithium-ion batteries. *Nat. Commun.* **10**, 3265 (2019).
59. L. Starukhina, Water detection on atmosphereless celestial bodies: Alternative explanations of the observations. *J. Geophys. Res.* **106**, 14701–14710 (2001).
60. L. V. Starukhina, Polar regions of the moon as a potential repository of solar-wind-implanted gases. *Adv. Space Res.* **37**, 50–58 (2006).
61. W. M. Farrell *et al.*, The statistical mechanics of solar wind hydroxylation at the Moon, within lunar magnetic anomalies, and at Phobos. *J. Geophys. Res.* **122**, 269–289 (2017).
62. D. H. Crider, R. R. Vondrak, Hydrogen migration to the lunar poles by solar wind bombardment of the moon. *Adv. Space Res.* **30**, 1869–1874 (2002).
63. Lunar Sample Preliminary Examination Team, Preliminary Examination of Lunar Samples from Apollo 11: A physical, chemical, mineralogical, and biological analysis of 22 kilograms of lunar rocks and fines. *Science* **165**, 1211–1227 (1969).